Digital image processing for wide-angle highly spatially-variant imagers

Stephen J. Olivas[a], Michal Šorel[c], Ashkan Arianpour[a], Igor Stamenov[a], Nima Nikzad[b], Glenn M. Schuster[a], Nojan Motamedi[a], William M. Mellette[a], Ron A. Stack[d], Adam Johnson[d], Rick Morrison[d], Ilya P. Agurok[a], and Joseph E. Ford[a]

[a]Photonic Systems Integration Laboratory, Electrical Engineering Department
[b]Computer Science and Engineering Department
University of California at San Diego, 9500 Gilman Dr., La Jolla, CA 92093, USA;
[c]Academy of Sciences of the Czech Republic, Institute of Information Theory and Automation, Pod Vodarenskou vezi 4, 18208, Prague 8, Czech Republic;
[d]Distant Focus Corporation, 4114B Fieldstone Road, Champaign, IL 61822, USA.

ABSTRACT

High resolution, wide field-of-view and large depth-of-focus imaging systems are greatly desired and have received much attention from researchers who seek to extend the capabilities of cameras. Monocentric lenses are superior in performance over other wide field-of-view lenses with the drawback that they form a hemispheric image plane which is incompatible with current sensor technology. Fiber optic bundles can be used to relay the image the lens produces to the sensor's planar surface. This requires image processing to correct for artifacts inherent to fiber bundle image transfer. Using a prototype fiber coupled monocentric lens imager we capture single exposure focal swept images from which we seek to produce extended depth-of-focus images. Point spread functions (PSF) were measured in lab and found to be both angle and depth dependent. This spatial variance enforces the requirement that the inverse problem be treated as such. This synthesis of information allowed us to establish a framework upon which to mitigate fiber bundle artifacts and extend the depth-of-focus of the imaging system.

Keywords: Spatially Variant, Extended Depth-of-Focus, Fiber Bundle Image Relay, Artifact Removal

1. INTRODUCTION - TRADITIONAL AND FIBER COUPLED IMAGERS

Commercially available image sensors are almost exclusively planar. This imposes constraints that negatively impact the overall imaging system performance by introducing aberrations and vignetting effects, especially off-axis.[1] Many of these problems can be avoided if the lenses can be designed to form an arbitrary geometric image surface. For example, a monocentric lens images without coma or astigmatic aberration and can significantly improve size, weight and performance (SWAP).[2–4] In our 30 MPix, 120° field-of-view prototype imaging system (Figs. 1(a) & 1(b)), fiber optic bundles are used to relay the spherical image surface to a flat image sensor. The system is comprised of a custom monocentric lens (f=12mm, F/#=1.35)[3,4] fabricated by Optimax (Fig. 1(c)), 2.5μm pitch fiber bundles manufactured by the Schott® corporation (for more information see[5,6]), and an Omnivision® OV5653 backside illuminated 5 megapixel color CMOS sensor with 1.75μm pixel pitch and image area of 4592μm wide by 3423μm high.[7] Monocentric lens imaging[8] and fiber optic bundle imaging[9,10] are not new ideas but there has been little research published on their impulse response, especially as it relates to digital processing to improve the raw images these systems produce. We investigated inherent problems relevant to any imaging system which uses fiber bundles to relay or field flatten an image surface onto flat CMOS/CCD image sensors (Fig. 1(d)). Detailed photos of the fiber bundle, and image sensor are shown along with a schematic of the fiber coupled sensor cross-section in Fig. 2. System impulse response measurements provide information that can be used to mitigate fiber optic bundle artifacts due to fiber sampling and defective fibers. We show a spatially variant deconvolution process[11,12] that uses focal swept images to extend the depth-of-focus of a

For further information: Send correspondence to Stephen J. Olivas; E-mail: stephenjolivas@gmail.com

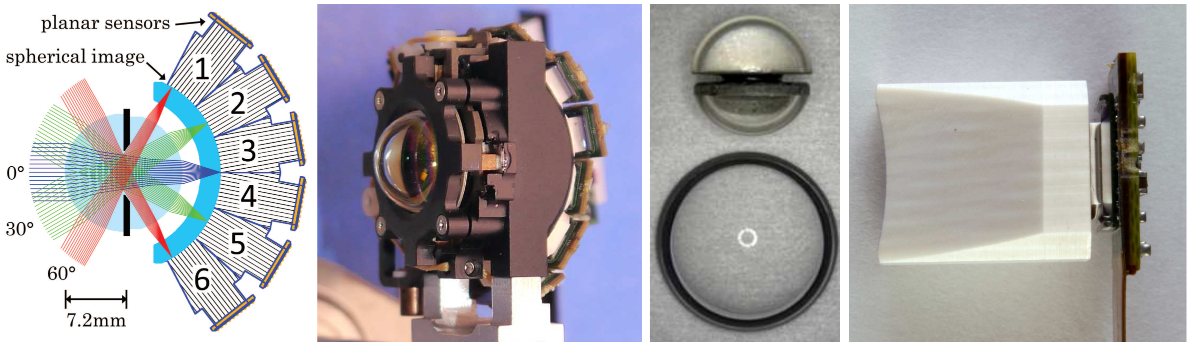

(a) Imager schematic (b) Prototype imager (c) MC lens (d) Fiber coupled sensor

Figure 1. (Color online) (a) Schematic of the prototype imager. A monocentric (MC) lens forms a low-aberration spherical image but requires a fiber bundle to relay the image to a flat sensor. (b) 30 MPix, 120° Fiber coupled monocentric lens prototype. (c) 2 glass monocentric lens. (d) Fiber bundle coupled to a sensor using UV cured epoxy.

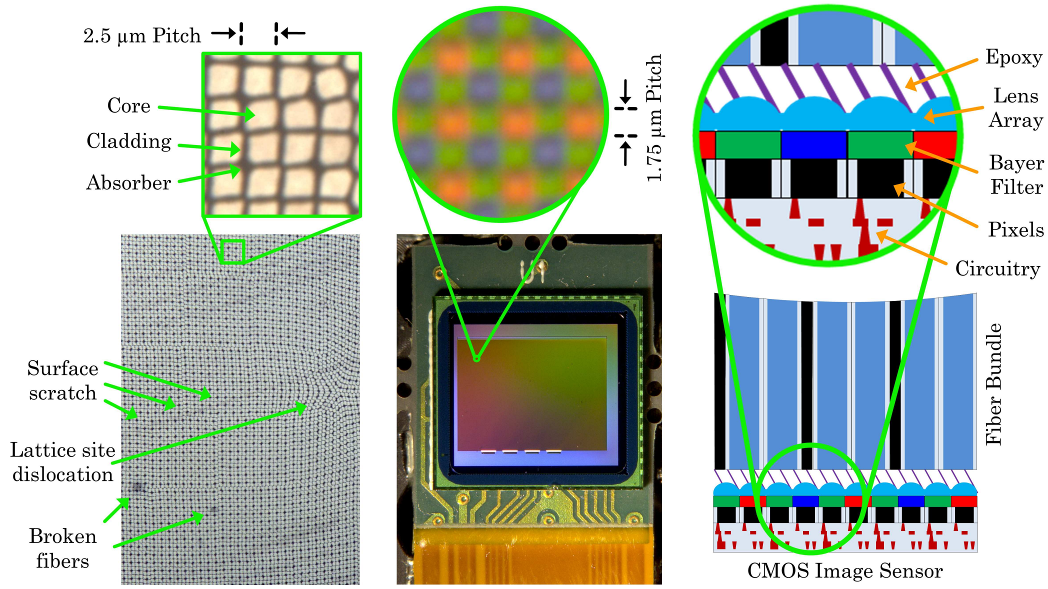

(a) Fiber bundle (b) CMOS sensor (c) Fiber coupled sensor schematic

Figure 2. (Color online) (a) Images showing fiber bundle structure and defects that lead to image artifacts. A fiber absorber is placed at every other $2.5\mu m$ fiber intersection to prevent crosstalk. (b) An Omnivision OVT5653 sensor. The two magnified micrographs in (a) and (b) are shown to scale. (c) Diagram showing the structure of the fiber bundle coupled sensor. The fiber bundle relays light incident at its surface to the CMOS image sensor though an epoxy bonding layer, lens array, and Bayer filter. The fiber bundle is coupled to an Omnivision sensor using UV cured Norland 72 epoxy.

wide field-of-view imager. Fig. 3 shows a side-by-side size comparison of the prototype camera and commercial camera.

Section 2 describes the flat-field calibration methods we employed to remove image artifacts due to fiber optic bundle image transfer and shows the before and after results made using outdoor images captured by our prototype imager. Section 3 explains the experimental setup used to measure the static depth-of-focus performance and to collect focal swept PSFs and images for extended depth-of-focus (EDOF) processing. Section 4 discusses the spatially variant EDOF algorithm and the resulting images the current EDOF system produces. Section 5 summarizes the fiber bundle artifact removal, the angle and depth dependent focal swept PSF measurements and the spatially variant EDOF imaging process.

Figure 3. (Color online) Photo showing the size comparison of the prototype camera and conventional camera.

2. FIBER COUPLED SENSOR ARTIFACT REMOVAL CALIBRATION

Here we present a method to experimentally gather a flat-field image from a fiber-coupled monocentric lens imager and use it for calibration. The flat-field image is an image taken of an evenly illuminated, uniform, unsaturated white target. This image reveals non-uniformities due to imperfections in the fiber coupled sensor. Using this flat-field image and a dark-field image we are able to compensate for different gains and dark currents within the pixels of a detector as well as the additional fixed pattern imparted on the image by the fiber bundle itself. This calibration is generally valid for the life of that system since it corrects for artifacts produced by the fiber bundle, epoxy bonding material and the sensor; all of which are permanently joined. The artifacts due to the epoxy adhesive as well as other materials that have properties that can vary with temperature, therefore multiple calibration maps can be collected to mitigate these effects. The artifacts are caused by cracked fibers, attenuation due to cladding and absorbing fibers, absorption due to the UV cured Norland optical adhesive NOA72 epoxy, and sampling effects between the bundle's fibers and the sensor's pixels. Sampling effects are produced when fibers and pixels are of comparable pitch leading to moiré patterns. There have been efforts to remove the fiber bundle effects related to image relay using techniques such as spatial filtering,[13] Gaussian smoothing,[14] or a Bayesian framework,[15] however they negatively impact the image resolution. The process here is similar to work presented in[14,15] with other obscuration/occlusion removal techniques documented in.[16–20] Fig. 4 shows (a) the flat-field calibration image, (b) an image taken of an outdoor scene, and (c) the corrected image. This result shows that the flat-field correction is extremely effective at reversing the negative effects introduced by the fiber bundle. The flat-field correction was made by element-wise division which compensated for attenuation of the signal. From the calibration images it appears that the fiber bundle does to not transfer light in certain locations and that there is total extinction of the light transmission due to broken fibers, however, even in the worst regions the attenuation was about half of the peak signal (see Fig 5). This allows us to use the calibration image to amplify all subsequent images. Areas which might not be remedied by this process, regions of the calibration image where signal was below a certain threshold, could be further corrected by interpolating to nearby regions but we found that this is not generally necessary. On a related note, interpolation of the Bayer color channels is of specific concern since many interpolation techniques are based on image continuity, which the raw fiber coupled image lacks. In this work, we selected bilinear interpolation from the many standard interpolation techniques we experimented with since it was most compatible with fiber coupled imaging.

3. EXPERIMENTAL SETUP

In order to produce data to perform and test the spatially variant extended depth-of-focus algorithm we configured the imager to take images both on and off axis using two fiber coupled sensors corresponding to sensors 4 and 6 in Fig. 1(a). One sensor imaged the scene from 0° on-axis to 20° and the other sensor imaged from 40° to 60°. The experimental lab scene we tailored to test the EDOF algorithm was setup to include targets placed at

(a) Flat-field calibration image shows artifacts and obscuration effects.
(b) Image taken outdoor with artifacts and obscuration effects present.
(c) Corrected image restored by amplification using the calibration image.

Figure 4. (Color online) (a) A flat-field calibration image of a uniform white scene shows artifacts due to broken fibers, scratches, and other imperfections as well as the fiber bundle's internal structure, all of which lead to artifacts in the acquired images. (b) A raw outdoor image exhibits degradation due to fiber bundle transfer. (c) Corrected image showing that the artifacts inherent to fiber bundle imaging can be corrected using a calibration image.

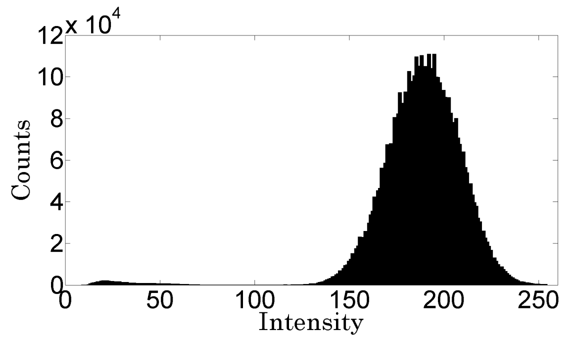

Figure 5. A histogram of a typical flat-field calibration image captured using a fiber coupled sensor. The lowest intensities transmitted by the fiber bundle are well above 100 on a 8-bit scale. The lower intensity values centered around an intensity of 25 correspond to a region of the sensor where there is no fiber bundle relay (no fiber bundle input signal) and can therefore be ignored. This enables us to use the calibration image to amplify the entire image in order to remove artifacts.

various distances (65cm, 83cm, 1m, 1.33m and 2m) perpendicular to the optical axis for each of the two angle ranges (Fig. 6 & 7). Ground truth images were taken with the camera focused to an on-axis orthogonal distance of 1m from the camera (Fig. 8). These images show that the depth-of-focus of the imager is limited to a certain depth surrounding the focus.

In order to extend the depth-of-focus we employ a swept focus method presented by Nayar et. al.[21] which relies on PSF depth independence, however we formulate the problem in a spatially variant framework in order to deal with the significant PSF dependence on field angle. The monocentric lens was mounted on a linear on-axis translation stage such that the focus could be swept during the capture of a single exposure (see inset of Fig. 6). The focal sweep corresponded to an object distance from 0.5m to infinite conjugate. The actuated

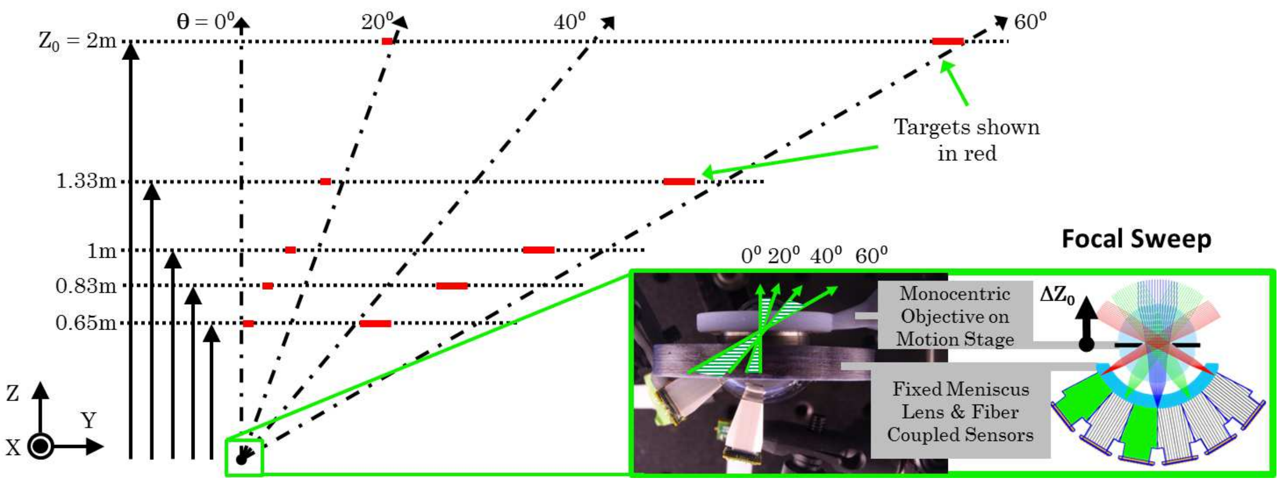

Figure 6. (Color online) Schematic of experimental setup and EDOF imaging system.

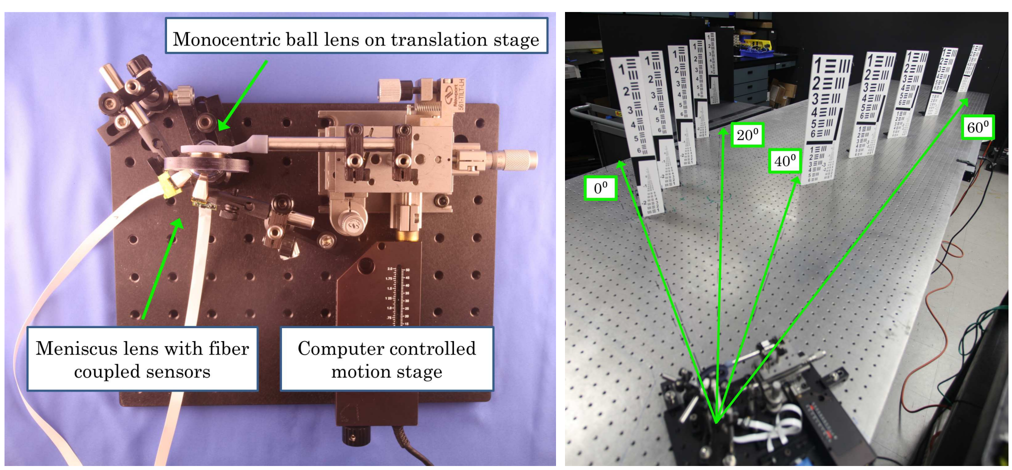

(a) Actuated system (b) Experimental setup

Figure 7. (Color online) Photo of EDOF imaging system and experimental lab setup.

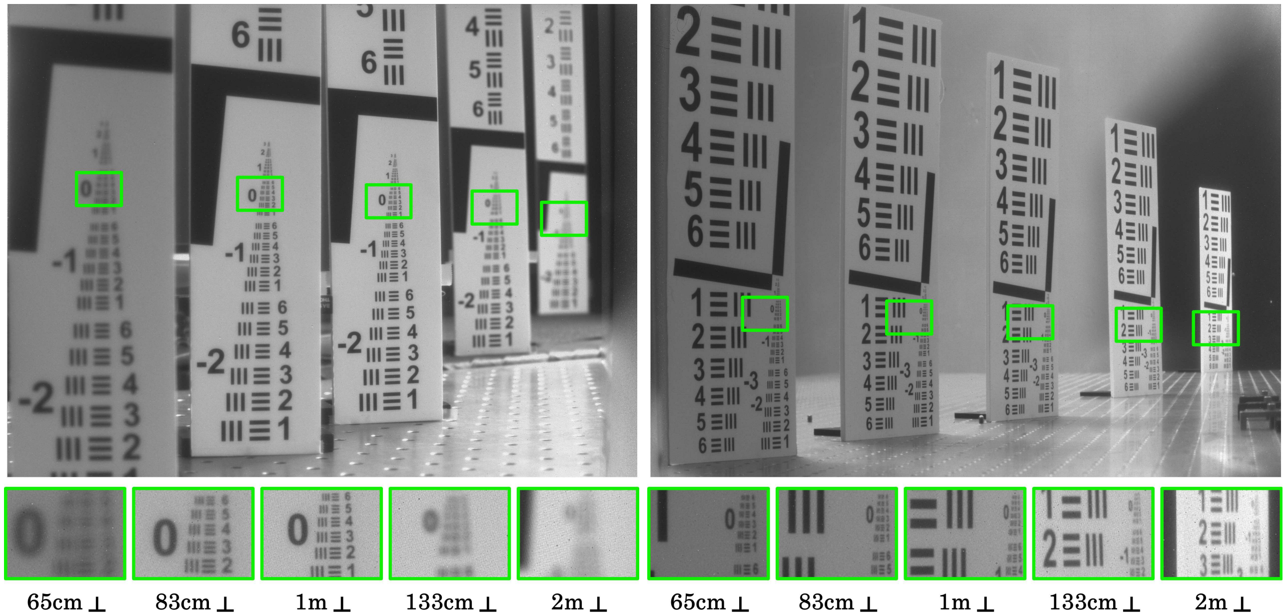

(a) Scene showing DOF for 0°-20°. (b) Scene showing DOF for 40°-60°.

Figure 8. (Color online) Image taken the with lens focused to 1m. Five targets are placed in the scene at depths of 0.65m, 0.83m, 1m, 1.33m, and 2m orthogonal to the optical axis. Magnified views show the limited depth-of-focus.

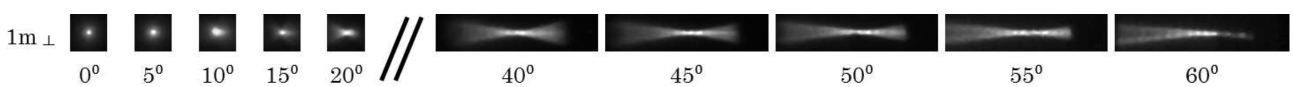

Figure 9. Single exposure focal swept images of a point source placed at 1m orthogonal along the optical axis for various field angles. This shows the PSF dependence on angle is significant and varies continuously.

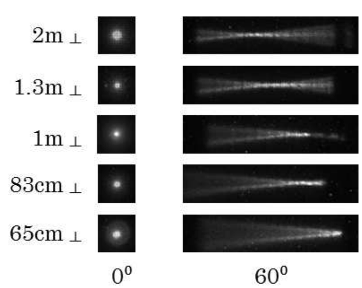

Figure 10. Single exposure focal swept images of a point source placed at 0° and 60° for a set of distances orthogonal to the optical axis. This shows that the on-axis PSFs are approximately independent of depth while the off-axis PSFs are highly dependent on depth.

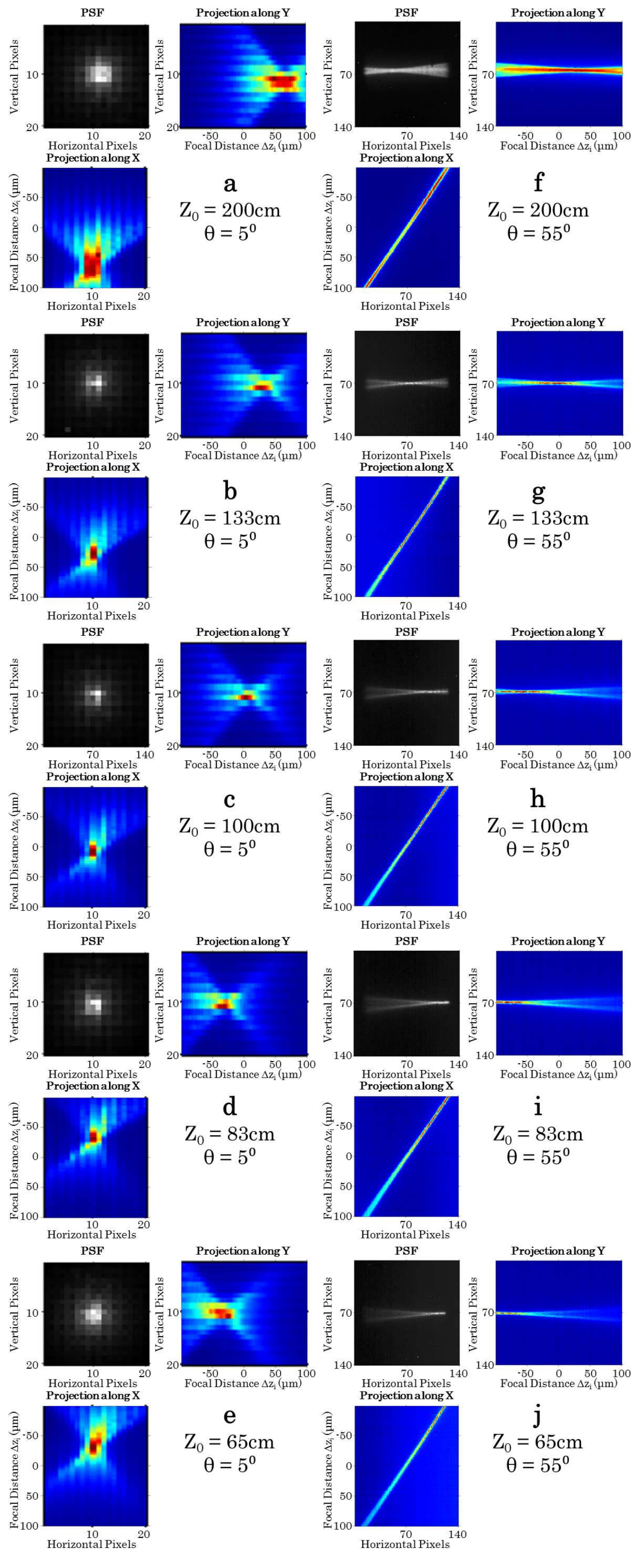

Figure 11. (Color online) The spatially variant PSF changes depending on object distance and angle (note PSF scale). Many exposures were taken as the EDOF system's focus was incrementally stepped. Profiles of the captured images as a function of focal position (intensity shown using false color plots) show that the behavior is different for the various depths. Integrated PSFs are shown in grayscale. However, the integrated on-axis PSFs (a-e) are substantially independent on scene depth whereas the off-axis PSFs (f-j) are greatly influenced by the distance of the point source.

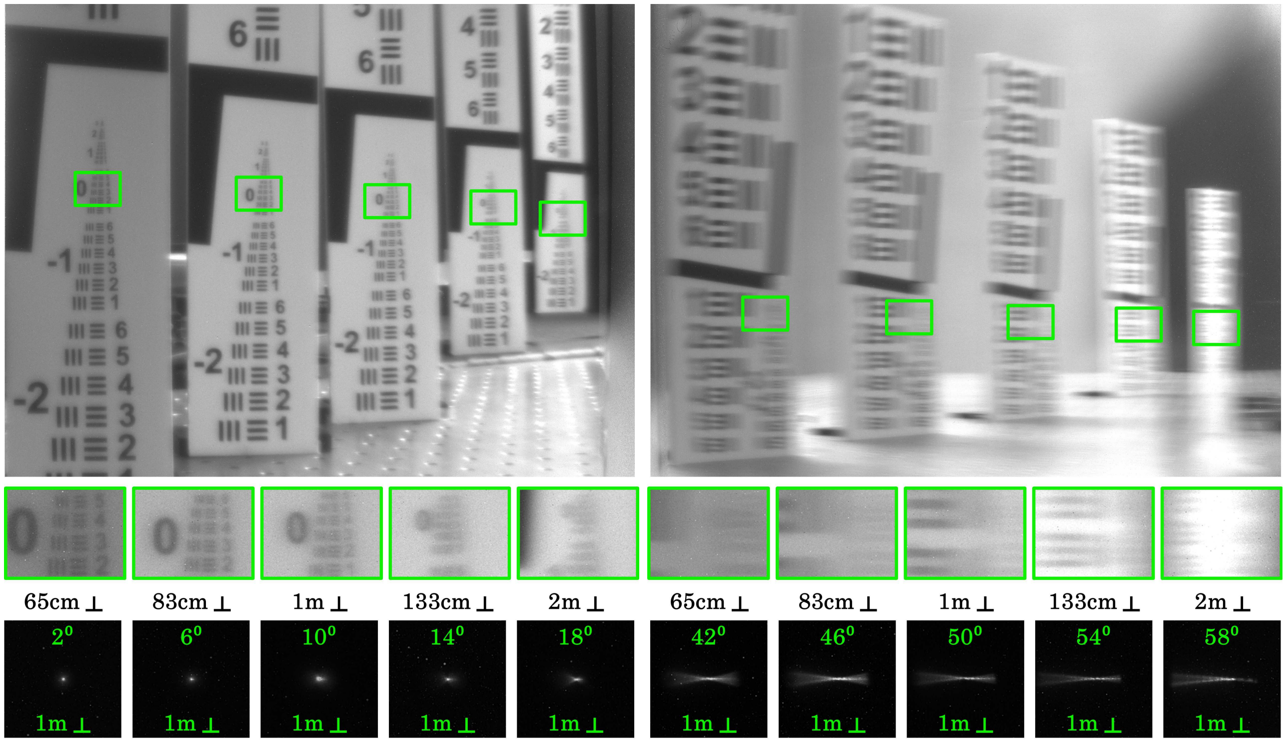

(a) Scene showing DOF for 0°-20°. (b) Scene showing DOF for 40°-60°.

Figure 12. (Color online) Single exposure focal swept images and PSFs. The focus is swept from 0.5m to infinite conjugate. Five targets are placed in the scene at depths of 0.65m, 0.83m, 1m, 1.33m, and 2m orthogonal to the optical axis. Magnified views show the extent of blur. Also shown are measured PSFs which exhibit more than 140 pixels of blur at high angles.

system was also used to capture single exposures of point sources placed at various angles across the scene (fixed orthogonal distance of 1m), see Fig. 9. This was done to measure PSFs as a function of field angle, which is later used in the spatially variant EDOF algorithm. That is that the spatially variant EDOF algorithm is based on angular dependent PSFs measured at a fixed orthogonal distance. Additionally we explored the system response to point sources at various object distances (field angle fixed to 0° and 60°), see Fig. 10. This data reveals that the idea that the PSF is relatively independent of depth is reasonable for on-axis images taken with the prototype, as was the case for the entire image collected by the substantially telecentric lens used in reference.[21] In other words, as the focus is swept, the distribution of light on the detector varies notably depending on the distance of the point source, however, the integrated swept intensity is approximately the same for point sources at different distances (see 0° PSF data in Fig. 10). Since the on-axis PSF is substantially depth independent, this allows conventional space invariant image processing techniques be used to extend the depth-of-focus of the image scene in the paraxial region. This is in stark contrast to the behavior of the integrated off-axis focal swept PSFs which exhibit significant depth dependence. This behavior is evident in the 60° data shown in Fig. 10. Even though the off-axis PSF is depth dependent, there is a range at which the EDOF algorithm can improve the system performance. In addition to the single exposure focal swept PSF measurements shown in Figs. 9 & 10, Multiple PSF exposures were taken as the focus stepped incrementally to show the PSF dependence on focal position during the focal sweep. This stepped PSF measurement investigation is summarized in Fig. 11. Although not experimentally explored here, this raises the possibility of performing depth dependent deblurring based on apriori scene information or a depth map captured using a low resolution stereo pair imager.

The fiber coupled monocentric lens prototype has the property that it focuses to an orthogonal object plane. In our experiments we used the 1m orthogonal distance to the camera as our central distance (Fig. 8). To extend the EDOF framework to wide angle images we must take into account the PSF variation as a function of field angle, see Fig. 9. Raw focal swept images and spatially variant PSF data (angle variant, fixed orthogonal depth) captured using the actuated EDOF are shown in Fig. 12. Using these PSFs, the raw focal swept image, the flat-field calibration image and the dark-field image we implemented a spatially variant EDOF image processing algorithm. This spatially variant deconvolution algorithm is described in the following section.

4. SPATIALLY VARIANT EXTENDED DEPTH-OF-FOCUS ALGORITHM

Here we present the spatially variant EDOF algorithm that was used to process the mechanically actuated focal swept imagery. This relies on solving (1) using a degraded image and measured spatially-variant PSF data (taken at various field angles with fixed orthogonal distance of 1m). The inset of Fig. 6 shows a schematic of the system along with a photo of the prototype.

$$z(x,y) = [Hu](x,y) = \int u(x-s, y-t)h(x-s, y-t; s, t)dsdt \tag{1}$$

Reconstruction of the original sharp image can be formulated in the Bayesian sense as seeking the maximally probable solution given certain assumptions on distributions of the noise and image u. A common choice of the image prior distribution is proportional to the total variation of image gradient $\int |\nabla u|\, dxdz$. Assuming the Gaussian noise distribution, this is equivalent to minimizing the functional

$$\min_u \frac{1}{2} \|z - QHu\|^2 + \lambda \int |\nabla u| dxdy, \tag{2}$$

where Q is a diagonal operator $Q : R^2 \to [0, 1]$ representing multiplication by an attenuation factor in each pixel, H the operator of space-variant convolution[11,12] $H : R^2 \to R^2$ and $z : R^2 \to R^+$ is the observed image we obtain from the image sensor. The attenuation factor Q is used here if the focal swept image has not been flat-field corrected by the method described in section 2.

There are many numerical methods to minimize (2). We have chosen an iterative solution, where in each iteration, the functional is replaced by its quadratic majorant

$$u_{n+1} = \arg\min_u \frac{1}{2} \|z - QHu\|^2 + \lambda \int \frac{|\nabla u|^2}{2\max(\varepsilon, |\nabla u_n|)} dxdy. \tag{3}$$

The absolute value in the denominator of (3) is constrained to be above 2ε to avoid division by zero. This measure can be also interpreted as replacing the non-differentiable absolute value in (2) by the Huber function.

The EDOF image resulting from the implementation of this algorithm on the experimentally obtained laboratory data is shown in Fig. 13. These preliminary results show the algorithm is mathematically operational and produces deblurred reconstructions of the focal swept images in Fig. 12. When compared to the swept focal images, the near-axis image depth-of-focus is improved and the off-axis image shows improved lateral resolution at a broader range of depths. However, the objective is to demonstrate an improved the depth-of-focus when compared to the static images in Fig. 8. The 0°-20° reconstructed image does seem to have sharper edges, but upon closer inspection there is no resolution gain over the range of depths. The 40°-60° reconstructed image is much worse than the image taken with a static focus. Three possible causes as to why the current system is not performing up to its expectations include the following reasons. Repeatability of the actuated system can directly influence the reconstructions because the PSF measurements must coincide with the focal swept data. Since the two are not measured simultaneously this can be a cause for concern. A second possible cause is the large number of pixels over which the PSF extends in detector space. The size of the PSF is over 40 pixels for the on-axis image and over 120 pixels for the off-axis image. This leads to complications when implementing the algorithm. A third possible cause can be the amount of noise in the imagery. As with a large PSF, noise leads to severe errors in the solution of inverse problems such as the one formulated here. The noise introduced into the system is caused by the need to capture long exposure images in order for the actuation system to produce repeatable motion. The shortest feasible exposure time in our current system is on the order of 2 seconds. This

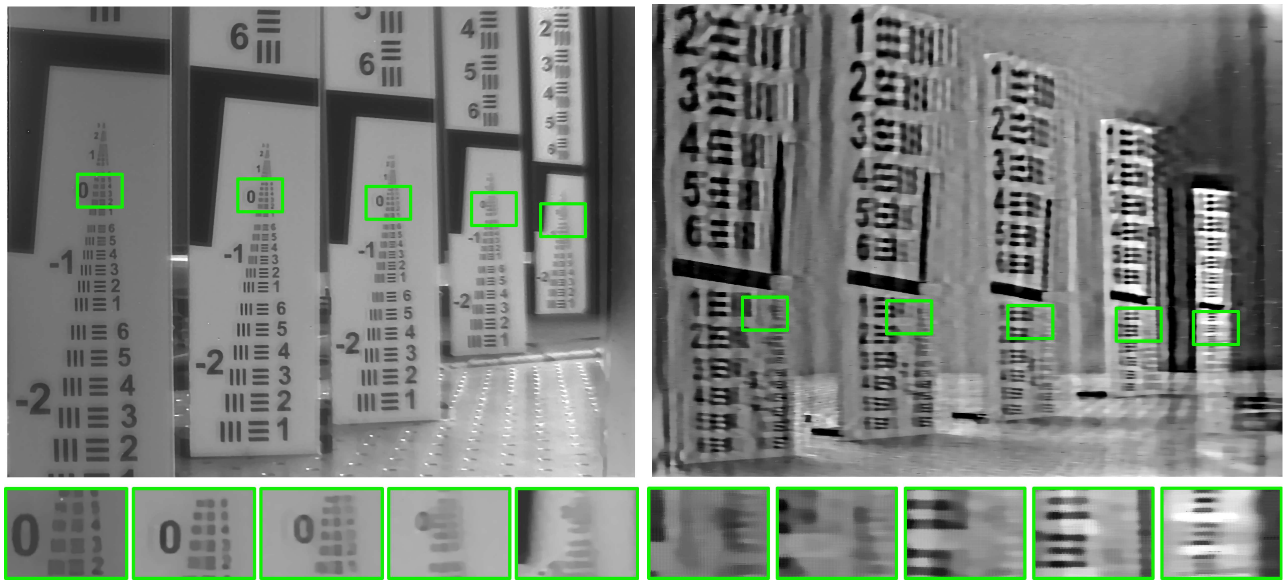

(a) Scene reconstruction showing DOF for 0°-20°. (b) Scene reconstruction showing DOF for 40°-60°.

Figure 13. (Color online) EDOF image processed using the spatially variant PSF data and focal swept imagery in Fig. 12. Magnified views from the various seen depths show the depth-of-focus of the processed image.

produces imagery with substantial noise causing the EDOF results to suffer. A future prototype design involves the use of a voice coil actuator in order to induce a sinusoidal oscillation of lens so that the integration time of the sensor can be brought down to tenths of a second or less. During this short exposure time the focus would oscillate multiple times enabling a spatially variant EDOF system that is less susceptible to noise.

5. DISCUSSION & CONCLUSION

We demonstrated how flat-field correction proves exceptionally beneficial for fiber coupled imaging systems since it corrects for obscuration and non-uniformity in the response of the lens, fiber bundle and sensor. More generally we have described a systematic process for reducing image degradation for fiber bundle image transfer between non-planar surfaces, a technique useful for multiple applications that in some cases would otherwise be impractical. We supported this idea by correcting experimentally collected outdoor images, and showing that this step is essential in removing fiber bundle artifacts and correcting vignetting effects. We used this methodology to generate wide field-of-view fiber coupled images with less distortion than those produced by traditional retro-telephoto "fish-eye" lens imagers. We went on to establish a framework to create spatially variant extended depth-of-focus images using single exposure images taken synchronously with a mechanical focal sweep. In order to investigate the problem and process the raw focal swept images, we performed an in-depth study of the dynamic behavior the PSF exhibits as a function of both scene angle and depth. We found that near the optical axis (which is along the direction of the focal sweep) the PSFs were depth independent; off-axis this was depth invariance did not hold. We presented a mathematical framework to process spatially variant extended depth-of-focus images using focal swept image and PSF data. We presented preliminary results which remains a topic of ongoing research.

ACKNOWLEDGMENTS

This work was supported by the DARPA SCENICC program under contract W911NF-11-C-0210. Michal Šorel was partially supported by the Grant Agency of the Czech Republic under project 13-29225S.

REFERENCES

[1] Seung-Bum Rim, Peter B. Catrysse, Rostam Dinyari, Kevin Huang and Peter Peumans, "The optical advantages of curved focal plane arrays," Opt. Express, **16** (7), 4965–4971 (2008).

[2] Stephen J. Olivas, Nima Nikzad, Igor Stamenov, Ashkan Arianpour, Glenn Schuster, Nojan Motamedi, William M. Mellette, Ronald A. Stack, Adam R. Johnson, Rick Morrison, Ilya Agurok and Joseph E. Ford, "Fiber Bundle Image Relay for Monocentric Lenses," Computational Optical Sensing and Imaging, OSA Technical Digest, paper CTh1C.5 (2014).

[3] Joseph Ford, Igor Stamenov, Stephen J. Olivas, Glenn Schuster, Nojan Motamedi, Ilya P. Agurok, Ron Stack, Adam Johnson and Rick Morrison, "Fiber-coupled Monocentric Lens Imaging," Imaging and Applied Optics Technical Papers, OSA Technical Digest, paper CW4C.2 (2013).

[4] Igor Stamenov, Ilya P. Agurok and Joseph E. Ford, "Optimization of two-glass monocentric lenses for compact panoramic imagers: general aberration analysis and specific designs," Appl. Opt., **51** (31), 7648–7661 (2012).

[5] Schott® "Fiber Optic Faceplates," http://www.us.schott.com/lightingimaging/english/download/faceplate_us_july_2013.pdf.

[6] Jed J. Hancock, *The Design, Fabrication, and Calibration of a Fiber Filter Spectrometer*. The University of Arizona, (1957).

[7] Omnivision® "OV5653 Color CMOS QSXGA Image Sensor with OmniBSI technology," OV5653-A66A datasheet, Oct. 2011. http://www.ovt.com/products/sensor.php?id=68.

[8] Rudolf Kingslake, *A History of the Photographic Lens*. Academic Press, (1989), pp. 49-67.

[9] Narinder Singh Kapany, James A. Eyer and Robert E. Keim, "Fiber Optics. Part II. Image Transfer on Static and Dynamic Scanning with Fiber Bundles," J. Opt. Soc. Am., **47** (5), 423–425 (1957).

[10] Renee Drougard, "Optical Transfer Properties of Fiber Bundles," J. Opt. Soc. Am., **54** (7), 907–907 (1964).

[11] Stephen J. Olivas, Michal Šorel and Joseph E. Ford, "Platform motion blur image restoration system," Appl. Opt., **51** (34), 8246–8256 (2012).

[12] Stephen J. Olivas, Michal Šorel, Nima Nikzad and Joseph Ford, "Platform motion blur image restoration system," Imaging and Applied Optics Technical Papers, OSA Technical Digest, paper CTu2B.3 (2012).

[13] Molly M. Dickens, Michael P. Houlne, Sunanda Mitra, and Darryl J. Bornhop, "Method for depixelating micro-endoscopic images," Optical Engineering, **38** (11), 1836–1842 (1999).

[14] Jae-Ho Han, Junghoon Lee and Jin U. Kang, "Pixelation effect removal from fiber bundle probe based optical coherence tomography imaging," Opt. Express, **18** (7), 7427–7439 (2010).

[15] Jae-Ho Han and Sang Min Yoon, "Depixelation of coherent fiber bundle endoscopy based on learning patterns of image prior," Opt. Lett., **36** (16), 3212–3214 (2011).

[16] Cormac Herley, "Automatic occlusion removal from minimum number of images," 2005 IEEE International Conference on Image Processing 2, II-1046-9 (2005).

[17] Jinwei Gu, Ravi Ramamoorthi, Peter Belhumeur and Shree Nayar, "Removing image artifacts due to dirty camera lenses and thin occluders," ACM Trans. Graph., **28** (5), 144:1–144:10 (2009).

[18] Devasruthi D, Hema P. Menon and Kotheneth A. Narayanankutty, "FE-BEMD and Exemplar based Hybrid Image Inpainting for Occlusion Removal," International Journal of Computer Applications, **28** (8), 38–44 (2011).

[19] Scott McCloskey, Michael Langer, and Kaleem Siddiqi, "Removal of Partial Occlusion from Single Images," IEEE Transactions on Pattern Analysis and Machine Intelligence, **33** (3), 647–654 (2011).

[20] Bincy Antony M and Kotheneth A. Narayanankutty, "Removing Occlusion in Images using Sparse Processing and Texture Synthesis," International Journal of Computer Science, Engineering and Applications (IJCSEA), **2** (3), 117–124 (2012).

[21] Hajime Nagahara, Sujit Kuthirummal, Changyin Zhou and Shree K. Nayar, "Flexible Depth of Field Photography," European Conference on Computer Vision (ECCV), (2008).